Journal of Materials Science & Technology 44 (2020) 48–53

Contents lists available at ScienceDirect

Journal of Materials Science & Technology

journal homepage: www.jmst.org

Research Article

In-situ surface transformation of magnesium to protect against oxidation at elevated temperatures

Yuecun Wang[a], Meng Li[a], Yueqing Yang[a], Xin'ai Zhao[a], Evan Ma[b,*], Zhiwei Shan[b,*]

[a] Center for Advancing Materials Performance from the Nanoscale (CAMP-Nano) & Hysitron Applied Research Center in China (HARCC), State Key Laboratory for Mechanical Behavior of Materials, Xi'an Jiaotong University, Xi'an, 710049, China
[b] Department of Materials Science and Engineering, Johns Hopkins University, Baltimore, 21218, MD, USA

ARTICLE INFO

Article history:
Received 8 August 2019
Received in revised form
25 September 2019
Accepted 7 October 2019
Available online 8 January 2020

Keywords:
Magnesium
Thermal oxidation
In-situ E-TEM
Carbonation
Oxidation inhibition

ABSTRACT

The native oxide thin scale on magnesium (Mg) surface appears continuous and crack-free, but cannot protect the Mg matrix from further oxidation, especially at elevated temperatures. This thermal oxidation process is witnessed in its entirety using a home-made *in-situ* heating device inside an environmental electron transmission microscope. We proposed, and verified with real-time experimental evidence, that transforming the native oxide scale into a thin continuous surface layer with high vacancy formation energy (low vacancy concentration), for example $MgCO_3$, can effectively protect Mg from high-temperature oxidation and raise the threshold oxidation temperature by at least two hundred degrees.

1. Introduction

Magnesium (Mg) is the lightest structural metal, with high specific strength, high electrical/thermal conductivity, good damping capacity, and recycling potentials. Mg alloys therefore have broad application prospects in transportation and aerospace industry [1–4]. Indeed, the incessant push for weight reduction of vehicles is calling for more and more use of Mg alloys. However, Mg has very high affinity to oxygen, especially at elevated temperatures [5]. The high reactivity of Mg leads to severe oxidation, causing surface degradation, loss of material or even fire hazards [6]. The integrity and durability of Mg alloys during service or processing at above 200 °C (e.g., casting, hot forming, heat treatment cycles, and welding [7–9]) is therefore a serious problem awaiting solution [5,6,10].

In dry oxidizing atmospheres, MgO is the dominant oxidation product. At ambient temperature, the initial oxide scale formed on Mg surface exposed to air appears continuous and crack-free, with a thickness of a few nanometers [11,12]. However, different from the passive films that form on aluminum or titanium, the Mg's native oxide scale is non-protective, especially in high-temperature oxygen-containing or humid environments [2,12]. Therefore, understanding the failure mechanism of the native oxide scale is crucial. At temperatures below ~400 °C, Mg oxidation is primarily mediated by the outward diffusion of Mg^{2+} ions from the metal-oxide interface to the oxide-air interface [2]; at higher temperatures, catastrophic oxidation enhanced by local melting or sublimation takes place [13,14]. MgO ridges grow from oxide cracks and distribute over Mg surface nonuniformly, forming a cauliflower-like morphology [10,15,16]. To reduce the high-temperature oxidation, other reactive elements with high affinity to oxygen are often alloyed into Mg surface or bulk. Examples are Ca, Be, and some rare earth elements (e.g. Y, Ce, La, Gd, etc.) [15]. They improve the oxidation resistance by promoting the formation of compact oxide barrier layers, affecting the oxidation kinetics in early stages or changing the MgO growth mechanism. Higher concentrations may better suppress oxidation [15,17], but high Ca or Be additions can increase brittleness, grain coarsening or hot cracking in some Mg alloys [18–20]. As for the rare earth elements, there are issues with their relatively high cost and low availability. Innovative treatments are therefore desired for protection against oxidation.

Recently, *in-situ* electron transmission microscopy (TEM) has shown advantages in directly monitoring the oxidation of Mg [13,21], over previous characterization methods including thermogravimetric analysis [22], XPS [5], and Auger electron spectroscopy [10]. Zhang *et al.* reported the *in-situ* thermal oxidation of Mg

* Corresponding authors.
E-mail addresses: ema@jhu.edu (E. Ma), zwshan@mail.xjtu.edu.cn (Z. Shan).

https://doi.org/10.1016/j.jmst.2019.10.018
1005-0302/

nanoparticles carried out inside an environmental TEM (E-TEM) [13] under an ultra-low oxygen pressure of $\sim 8 \times 10^{-2}$ Pa at two specific temperatures. However, their focus was not on the initial oxidation stages involving the damage of the native oxide scale, not to mention a new methodology to suppress Mg oxidation at elevated temperatures. Here we carry out real-time observations of the entire Mg oxidation process at elevated temperatures under a higher oxygen pressure inside E-TEM, and find a way to carbonate the unreliable native oxide scale into a continuous and compact $MgCO_3$ layer. The resultant protective barrier effectively inhibits oxidation at high temperatures, as will be demonstrated in the following.

2. Experimental

Single crystals of nominally pure Mg (purity of 99.99 wt.%) were used in our experiments to avoid the complications from alloying elements and grain boundaries. The Mg disks were cut into $\sim 1 \times 2$ mm^2 rectangular plates that were then mechanically polished using abrasive paper. The $\sim 30 \times 15$ μm^2 rectangular lamellae with the thickness of ~ 2 μm were lifted out from the above plate using nano-manipulator and then transferred to the free-standing end of a home-made microelectromechanical system (MEMS) heating chip with sample mounting posts dedicated for FIB sample [23] (see Fig. S1). The Mg lamellae were welded to the sample mounting posts on the hotplate via platinum deposition. The whole lift-out process was carried out by the focused ion beam (FIB, FEI Helios 600, dual-beam FIB system, operating at 30 kV ion beam and 10 kV electron beam). After the transfer, cylindrical Mg micropillars were micromachined directly on the lamellae using 30 kV focused Ga^+ beam. The milling beam current for coarse cutting was sequentially decreasing from 600 pA to 93 pA, and the milling current for the last-step fine polishing was as low as ~2 pA so as to minimize the ion bombardment induced damage. All the magnesium pillars used for this experiment have the diameters of 100–200 nm and the aspect ratio (height to diameter) of 3–5.

The high resolution TEM image and electron energy loss spectroscopy (EELS) mapping of the magnesium/oxide interface were performed in a JEOL 2100 F TEM operated at 200 kV equipped with an EELS detector. Both the *in-situ* carbonation and heating experiments were carried out in a differential pumped environmental TEM (Hitachi H9500, 300 kV). The specimen chamber was evacuated to a base vacuum of $\sim 10^{-4}$ Pa. In the carbonation process, high-purity CO_2 (99.99%) was introduced into the specimen chamber through a needle valve. The pressure was controlled in the range of 2–4 Pa, which is measured by a Pirani vacuum gauge near the sample. The specimens were kept at room temperature (~20 °C) during the carbonation process. The formation rate of $MgCO_3$ can be tuned by adjusting the electron-beam intensity. In our experiments, the beam intensity for carbonation was ~0.1 A·cm^{-2} and that for normal illumination was ~0.02 A·cm^{-2}. The heating process was performed in 2–4 Pa ultra-high-purity O_2 (99.999%) atmosphere using a home-made heating stage at the heating rate of 1 °C–5 °C min^{-1}. The electron beam intensity during the high-temperature oxidation was controlled below ~0.02 A·cm^{-2}.

3. Results and discussion

3.1. In-situ *oxidation of Mg pillars at elevated temperatures*

The Mg micropillars were fabricated in cylindrical shape (Fig. 1(a)) to allow an edge-on view of the specimen surface, facilitating the real-time imaging in TEM. The pillar taken from the FIB vacuum chamber was then exposed to dry air (relative humidity: < ~1%) for two days to develop a native oxide scale. Fig. 1(b and c) show the high-resolution TEM image of a typical Mg pillar and the corresponding EELS mapping of the magnesium-oxide interface, respectively. The native oxide layer is amorphous with a thickness of ~5 nm, in agreement with previous observation that the oxide formed on Mg at ambient temperature is amorphous rather than crystalline [11,15]. According to Czerwinski [11], the initial oxide has an oxygen deficiency (Mg to O ratio larger than 1:1). To reach the full stoichiometry of MgO, growth at high temperature is required. The native oxide on the Mg pillar at room temperature appears continuous and dense, because it is sufficiently thin to sustain the mismatch between the oxide and the base metal.

Thermal oxidation was then performed inside the E-TEM using the home-made MEMS heater that has accurate temperature control and minimized thermal drift. Pure oxygen gas was injected into the chamber to a constant pressure of ~4 Pa. Afterwards, the sample was heated from room temperature (20 °C) to 200 °C under a constant heating rate of 1 °C min^{-1}. Fig. 2(a) shows the snapshots from the *in-situ* video (Supplementary movie 1) recording the dynamic oxidation process of a typical example during temperature ramping. Clearly, we see that at the beginning of oxidation the native oxide thin scale on the pillar surface is thin, uniform and crack-free. But with increasing temperatures, nanometer-sized voids appear in the oxide scale, and they grow in size gradually along with the thickening oxide scale. Then, cracks open up inside the oxide scale, initiating from the voids, and meanwhile oxygen penetrates inward reacting with fresh Mg at cracks. At temperatures above 120 °C, oxidation becomes fast and increasingly out of control, and eventually the whole pillar becomes spongy with many oxide ridges distributed on its surface. The degree of oxidation, and the morphology of the oxide ridges formed in the presence of cracks, depends on the size of the cracks and the rate of their healing (filling cracks with the newly grown oxide). The number of ridges increases with temperature. At 200 °C, the pillar was almost entirely oxidized. The inset selected area electron diffraction patterns (SAEDP) in Fig. 2 show that the oxidation product is MgO [11].

Based on previous work on bulk magnesium [2,5,11,15,24] and our observations, the thermal oxidation mechanism can be summarized schematically in Fig. 2(b)): i) oxygen is adsorbed on the outer surface of the native oxide. At low temperatures, it is difficult for oxygen to penetrate through the adherent native oxide and react with the inner metal, and meanwhile the outward diffusion of Mg^{2+} ions is slow. Therefore, the oxidation rate is very low. ii) With increasing temperature, the diffusion-controlled growth of oxide takes place. Diffusion and transport of ions in solids occur resulting from the occurrence of structural defects. In MgO, the typical point defects are Schottky defects, which form in the lattice containing the oppositely charged Mg^{2+} cations and O^{2-} anions, when both types of ions leave lattice sites and create vacancies [25]. At this stage, thickening of the oxide layer is primarily governed by the outward sold-state diffusion of Mg^{2+} ions mediated by vacancies, from the metal-oxide interface to the oxide-gas interface to react with oxygen. The accompanying inward flux of cation vacancies generate voids at the metal-oxide interface, which then act as easy channels to cause fast diffusion of Mg^{2+} ions. iii) As oxidation proceeds, tensile stresses develop because of the accumulation of above-mentioned defects as well as the density difference between the thickening MgO layer and the Mg substrate (Pilling-Bedworth ratio [26] of MgO is ~ 0.8). When the internal stress is sufficiently high, cracks open up inside the oxide scale, initiating from the voids. This provides easy pathways for inward penetration of oxygen and outward Mg vapor (or liquid) diffusion to the surface. Since the pressure in the E-TEM chamber is far below the triple point pressure (333 Pa [27]), Mg directly sublimates from solid to vapor above the critical temperature. In other words, the oxide morphological changes are accompanied by the change in the oxidation mechanism from solid diffusion-controlled to chemical reaction-

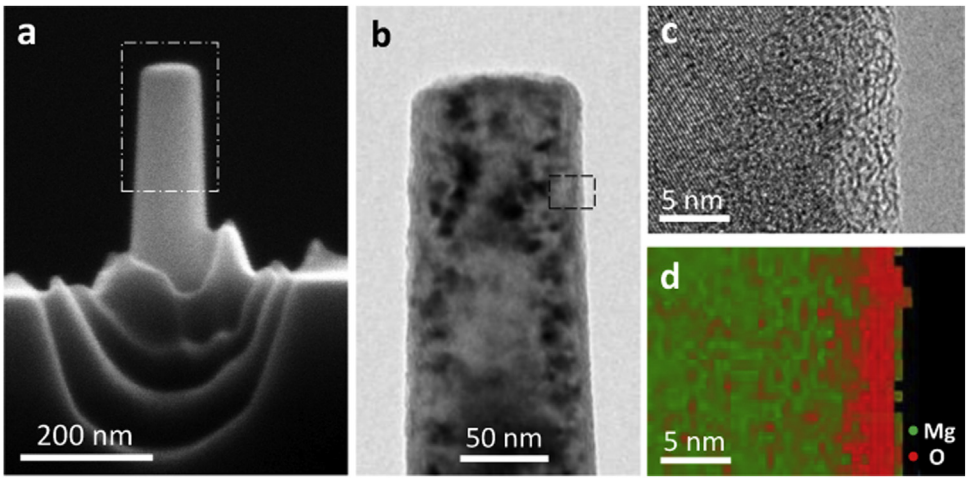

Fig. 1. Sample information. (a) SEM sideview image of a typical magnesium pillar with the diameter of ~ 100 nm. (b) Bright-field TEM image of the pillar framed by white dashed rectangle. (c) High resolution TEM image and the corresponding EELS mapping (d) of the magnesium-oxide interface, indicated by the black dashed frame in (b).

controlled. Subsequently, fresh MgO ridges grow up rapidly at the cracks, and the oxide layer loses its integrity. iv) The incessant growth of the oxide ridges with porous structure consumes more and more magnesium metal, gradually engulfing the entire pillar with thick spongy MgO. For bulk magnesium, such catastrophic oxidation causes the cauliflower-like surface morphology [16].

To quantify the oxidation kinetics of Mg pillar held in ~4 Pa oxygen, at each temperature interval the oxide thickness is plotted versus holding time in Fig. S2. Below 100 °C, the growth rate of MgO is very slow: the measured average growth rate is only 0.03 nm min^{-1}. The oxidation at 100 °C–150 °C follows the parabolic kinetics, and this stage precedes the nodular oxide growth at 180 °C–200 °C. This latter stage is fast and exhibits linear kinetics, where the measured slope becomes as high as ~0.85 nm·min^{-1}. Noted that besides elevating temperature, extending the holding time at a constant temperature makes the thermal oxidation of magnesium sustained as well. More details can be found in Supplementary Materials Fig. S3.

3.2. $MgCO_3$ scale transformed from the surface oxide protecting Mg from thermal oxidation

The discussion above indicates that the outward migration of Mg^{2+} ions causes the failure of native oxide scale and controls the oxidation progress. This, together with Pilling-Bedworth (P—B) ratio <1 for MgO, are responsible for the non-protective thermal oxidation of Mg. The Mg^{2+} ions migration rate is determined by the Mg^{2+} and O^{2-} vacancy density [28]. In MgO, the energy cost of Mg or O leaving lattice site to create a vacancy (formation of Schottky defect) was calculated to be < 6.7 eV [25]. Therefore, to suppress the oxidation of Mg at elevated temperatures one effective way would be to transform the initial surface oxide into some other magnesium compound with a high Schottky defect formation energy and meanwhile a P—B ratio larger than 1. After plenty of literature research, we found that $MgCO_3$ can be a suitable candidate because it has several desirable features [29–32]. First of all, $MgCO_3$ is sufficiently stable and compact ($MgCO_3$ growing on Mg would have a P—B ratio of 2.04). Second, in the crystal lattice of $MgCO_3$, the CO_3^{2-} anion with a large radius is a covalently bonded molecular unit and interacts mainly ionically with Mg^{2+} cations. In $MgCO_3$, the formation energy of Schottky defect (involving both a Mg vacancy and a carbonate vacancy) is as high as ~43 eV [30], six times that in MgO. Third, $MgCO_3$ seems to be a good protective barrier for Mg and its alloys from aqueous corrosion [29]. In principle, $MgCO_3$ can be obtained via the chemical reaction, $MgO + CO_2 \rightarrow MgCO_3$. The Gibbs free energy change of this chemical reaction has a negative value of -21.4 kJ·mol^{-1}, i.e., the process is thermodynamically favorable at ambient temperature. However, kinetically, for this reaction to occur at atmospheric pressure, heating to at least 400 °C is required [33]. This temperature is too high to be applied for Mg, considering its poor oxidation resistance and low melting point of 650 °C. But interestingly we have recently discovered that the excited CO_2 can make this carbonation readily happen at room temperature, and this excitation can be realized when CO_2 is under either high-energy electron beam or glow discharge [34].

Next, we use *in-situ* E-TEM experiment to demonstrate that the air-formed oxide scale on Mg can indeed be carbonated into a smooth, continuous and compact $MgCO_3$ surface layer at room temperature, and the $MgCO_3$ scale formed this way completely alters the oxidation behavior of magnesium at elevated temperatures. The Mg pillars used have dimensions and exposure times similar to those in Fig. 2. The SAEDP of one typical example in Fig. 3(a) identifies the surface native oxide as amorphous MgO. The pillar was then carbonated under the electron beam inside E-TEM with ~4 Pa pure CO_2 at room temperature. The CO_2 source was cut off, when the carbonation-induced morphological change became no longer obvious in the TEM image. At this point the outer scale is composed of newly-formed crystalline $MgCO_3$ with minor remnant crystallized MgO, as indicated by the corresponding SAEDP (Fig. 3(b)). This scale is of almost the same thickness as the MgO layer before carbonation, but is now more compact and continuous.

Then, the pillar with $MgCO_3$ scale was heated in ~4 Pa oxygen from room temperature to 350 °C; during the whole process the pillar appeared to be intact with no sign of the violent growth of MgO ridges (see Fig. 3(c)). Besides, the SAEDP and dark-field TEM image taken at 250 °C suggests the $MgCO_3$ scale is stable with no indication of more MgO formation. Approaching 350 °C, the platinum connection between the magnesium lamella base and the hotplate became too weak to hold up; we had to stop further increasing the temperature. Holding at 350 °C for 30 min, the pillar showed no significant morphological change, which was confirmed in a separate scanning electron microscope (SEM) examination after the E-TEM experiment (Fig. S4). This is in stark contrast with untreated pillar, which oxidized catastrophically even at 150 °C (Fig. 2(a)). With no newly-formed MgO, the diameter of the carbonated pillars measured manually did not increase with temperature, as demonstrated by the red data points in Fig. 4. This suggests that the $MgCO_3$ scale as thin as the native oxide surface layer effectively inhibits the very early state oxidation of magnesium, i.e. the ions diffusion through structural defects, and keeps the

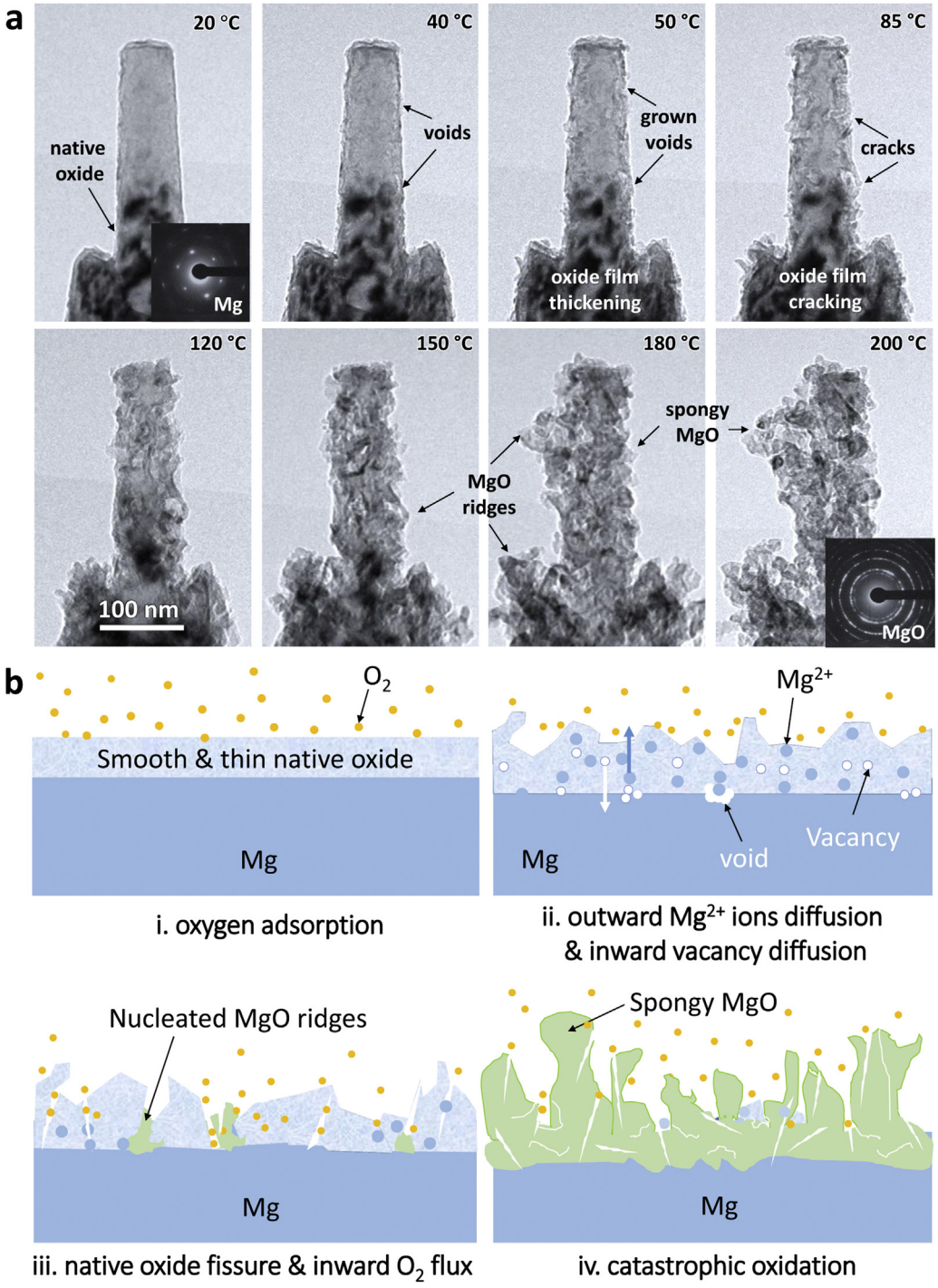

Fig. 2. Dynamic oxidation process and mechanism of Mg from room temperature to 200 °C. (a) TEM images showing the damage process of native oxide scale including the voids formation, voids growth and oxide scale cracking, as well as the following process of MgO ridges' growth from cracks at high temperatures. The inset selected area electron patterns indicate the initial magnesium pillar with a thin amorphous oxide surface layer is oxidized into MgO completely at 200 °C. (b) Sketches showing the thermal oxidation mechanism. i. Oxygen adsorbed on the native oxide surface at room temperature. ii. With increasing temperature, the outward Mg^{2+} ions diffusion channeled by the already existing vacancies is accelerated along with oxide scale thickening gradually. iii. The simultaneous inward vacancy diffusion leads to vacancy segregation forming voids, which, together with the tensile internal stress induced by the MgO scale thickening, cause crack formation in the oxide scale. Oxygen penetrates inward and reacts with fresh Mg at cracks. iv. Catastrophic oxidation occurs with fast MgO ridge growth forming a spongy morphology.

magnesium pillar free from oxidation at elevated temperatures. In comparison, the diameter of the untreated Mg pillars changes dramatically with temperature (black data points); the chemical reaction-controlled stage at higher temperatures shows a much higher slope compared with the diffusion-controlled oxidation at temperatures below 150 °C.

The drastic differences observed in E-TEM before and after carbonation indicate that $MgCO_3$ is a protective layer, highly effective in shutting off the diffusion mediated by vacancies and the fast diffusion channeled through cracks. This is because the compact $MgCO_3$ scale has a low vacancy density due to the high defect formation energy, and a high P-B ratio that gives rise to volume-

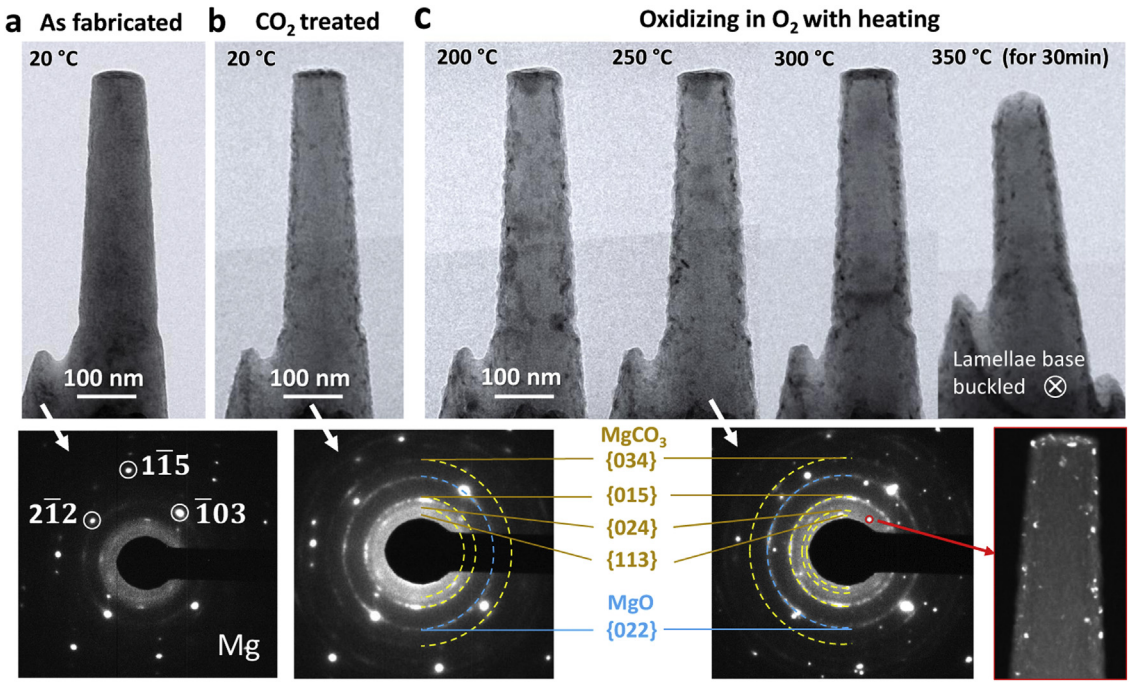

Fig. 3. Thermal oxidation inhibition effect of $MgCO_3$ scale directly transformed from the native oxide scale on the surface of magnesium. (a) Bright field TEM image and the corresponding SAEDP of a typical Mg pillar fabricate by FIB. (b) The pillar in (a) after carbonation inside E-TEM under 4 Pa CO_2 and electron beam irradiation. Its SAEDP illustrates that carbonated surface layer is composed of the newly formed $MgCO_3$ and some remained MgO, which are marked by the yellow and blue dashed curve, respectively. The main body of the pillar after treatment is still Mg crystal. (c) The carbonated pillar with $MgCO_3$ scale was heated from room temperature to 350 °C in ~4 Pa oxygen. At 250 °C, SAEDP was taken, and compared with the diffraction patterns in (b), it shows no obvious change. Chose one diffraction spot (marked by the red circle) from the {024} diffraction ring of $MgCO_3$ to take the corresponding dark-field TEM image (framed by red), showing that $MgCO_3$ mainly distributes on the surface. Approaching 350 °C, the TEM projection image of the pillar looks like shortened because the weld (connection of hotplate and magnesium lamella base) fracture at high temperatures. Actually, during the entire heating process in oxygen, the tested pillar kept intact and free from obvious oxidation.

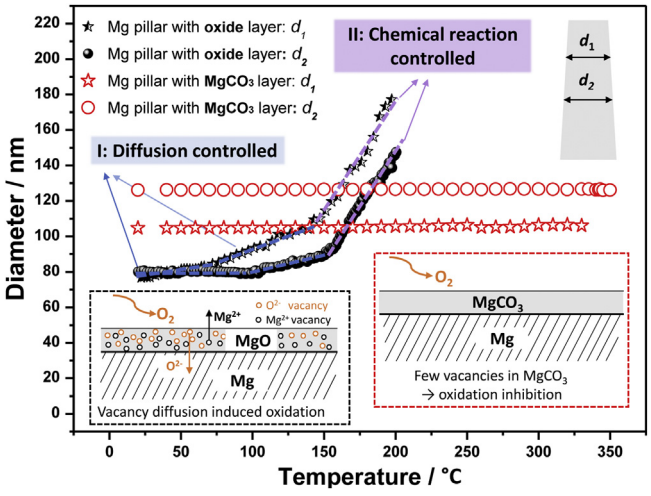

Fig. 4. Comparison of size changes of the untreated and carbonated magnesium pillars during the oxidation at different temperatures. For each pillar, the size changes of two different parts were measured (the top right inset schematic diagram). The black and red curves represent the size changes of the Mg pillar with native oxide layer and the Mg pillar with $MgCO_3$ scale, respectively. For the untreated pillar, its size changes dramatically along with temperature, and the changes themselves are temperature dependent, indicating the oxidation mechanism transforming from diffusion controlled to chemical reaction controlled. While, for the carbonated pillar, its size almost keeps a constant, suggesting no obvious oxidation. The inset schematics illustrate the vacancy diffusion induced initial oxidation of Mg with oxide layer (left, black) and the oxidation inhibition effect of $MgCO_3$ layer with few vacancies (right, red), respectively.

expansion induced compressive internal stresses. Therefore, there is no oxide layer thickening and cracking, let alone the wild growth of MgO ridges.

3.3. *Electron beam effect*

Finally, we comment on the electron beam effects on oxidation kinetics. Two identical Mg micropillars were compared, one exposed to the e-beam, and the other outside the field of view in the TEM. Both of them were heated to 200 °C in ~4 Pa oxygen and held for 40 min. We found that the pillar under the e-beam irradiation was oxidized seriously, covered with MgO nodules, similar to the cases shown earlier. In contrast, the other pillar far away from e-beam illumination only showed uniform oxide scale growth (see Fig. S5). The e-beam does promote thermal oxidation, making its onset earlier. At room temperature, this effect has not kicked in, as the pillar exposed to e-beam showed no visible oxidation (Fig. S6). Nevertheless, this e-beam acceleration effect does not affect the conclusion drawn from the comparison above: both cases, with and without carbonation, are subjected to the same electron irradiation in TEM, so the dramatic differences in oxidation behavior are not due to the e-beam effects.

As for the mechanism for electron irradiation effects, stoichiometry changes have been reported before in MgO [35]. E-beam induced oxide layer thickening by the enhanced surface diffusion was also found in metal nanoparticles [36]. Therefore, the e-beam irradiation enhanced thermal oxidation of magnesium with native oxide layer can be rationalized as e-beam stimulating Schottky

pair formation within MgO scale. The maximum energy transferred (E_{max}) by the 300 keV incident electrons to a Mg^{2+} ion and an O^{2-} ion is estimated using the elastic collision Kinchin-Pease model [37] to be 26.8 and 40.4 eV, respectively. The formation energy of Mg^{2+} and O^{2-} vacancy pair is only ~6.7 eV, and the calculated minimum acceleration voltage of the e-beam for creating the vacancy pair is about 70 kV. Therefore, the 300 kV e-beam could increase the vacancies concentration and hence accelerate the diffusion-controlled oxidation. In comparison, for $MgCO_3$, the E_{max} transferred by the 300 keV incident electrons to Mg^{2+} and CO_3^{2-} is 26.8 and 10.8 eV, respectively, lower than the Mg^{2+} and CO_3^{2-} vacancy pair formation energy (~43 eV). As such, the $MgCO_3$ scale is found intact and can protect the inner Mg from oxidation even when under e-beam irradiation at temperatures as high as 350 °C. Noted that the more expensive high-energy e-beam can be replaced by the non-thermal CO_2 plasma produced via glow discharge to obtain the excited CO_2 for the surface carbonation of macroscopic Mg alloys [34]. What's more, the $MgCO_3$ protective scale should be obtained from not only the native oxide layer but also the corroded surface of Mg alloys with the main components of MgO and $Mg(OH)_2$. Therefore, rather than having to mechanically clear away the prior corrosion products, one may directly convert them to a protective surface layer.

4. Conclusion

In summary, we have made real-time observations of the whole thermal oxidation process of Mg inside an E-TEM. The outward solid-state Mg^{2+} diffusion mediated by vacancies within the native oxide scale initiates the Mg oxidation and causes damage of the scale, followed by the catastrophic growth of MgO ridges from cracks of the oxide scale at increased temperatures. Via *in-situ* reaction with the excited CO_2 gas at room temperature, the native oxide scale on Mg surface is carbonated into a more compact $MgCO_3$ protective layer with higher vacancy formation energy and P-B ratio>1. The $MgCO_3$ layer is as thin as the initial oxide but can effectively protect Mg against oxidation at elevated temperatures. A drastic difference has been found in terms of oxidation rate and morphology, when comparing the native oxide surface versus the $MgCO_3$. In the latter case, the threshold temperature for severe oxidation has been increased by at least two hundred degrees. Considering MgO is the dominant component of the native surface of all magnesium-based alloys, the method described here is expected to be generally applicable to all types of magnesium alloys.

Acknowledgements

The authors gratefully acknowledge the support by the National Natural Science Foundation of China (51902249, 51621063) and National Key Research and Development Program of China (No. 2017YFB0702001), Science and Technology Department of Shaanxi Province (2016KTZDGY-04-03 and 2016KTZDGY-04-04). We also appreciate the support from the International Joint Laboratory for Micro/Nano Manufacturing and Measurement Technologies and the Collaborative Innovation Center of High-End Manufacturing Equipment and 111 project (B06025). Y.C. Wang was supported by the new faculty start-up funding from XJTU. EM acknowledges support from U.S. DoE-BES-DMSE, under Contract No. DE-FG02-16ER46056.

Appendix A. Supplementary data

Supplementary material related to this article can be found, in the online version, at doi:https://doi.org/10.1016/j.jmst.2019.10.018.

References

[1] T.M. Pollock, Science 328 (2010) 986–987.
[2] Q. Tan, A. Atrens, N. Mo, M.-X. Zhang, Corros. Sci. 112 (2016) 734–759.
[3] K.U. Kainer, B.L. Mordike, Magnesium Alloys and Their Applications, Wiley-VCH, Weinheim, 2000.
[4] M.M. Avedesian, H. Baker, ASM Specialty Handbook: Magnesium and Magnesium Alloys, ASM International, 1999.
[5] V. Fournier, P. Marcus, I. Olefjord, Surf. Interface Anal. 34 (2002) 494–497.
[6] Czerwinski F. Rijeka, Magnesium Alloys–Corrosion and Surface Treatments, InTech, Croatia, 2011.
[7] F.C. Campbell, Manufacturing Technology for Aerospace Structural Materials, Elsevier, New York, 2011.
[8] A.A. Luo, Int. Mater. Rev. 49 (2004) 13–30.
[9] D.J. Young, High Temperature Oxidation and Corrosion of Metals, 1st ed., Elsevier, 2008.
[10] C. Lea, C.J. Molinari, Mater. Sci. 19 (1984) 2336–2352.
[11] F. Czerwinski, JOM 64 (2012) 1477–1483.
[12] J. Nordlien, S. Ono, N. Masuko, K. Nisancioglu, Corros. Sci. 39 (1997) 1397–1414.
[13] Z. Zhang, X. Fu, M. Mao, Q. Yu, S.X. Mao, J. Li, Z. Zhang, Nano Res. 9 (2016) 2796–2802.
[14] F. Czerwinski, Acta Mater. 50 (2002) 2639–2654.
[15] F. Czerwinski, Int. Mater. Rev. 60 (2015) 264–296.
[16] T. Takeno, S. Yuasa, Combust. Sci. Technol. 21 (1980) 109–121.
[17] X.Q. Zeng, Q.D. W, L. Yizhen, Z. Yanping, D. Wenjiang, Z.J. Yunhu, Mater. Sci. Technol. 112 (2001) 17–23.
[18] P. Li, B. Tang, E. Kandalova, Mater. Lett. 59 (2005) 671–675.
[19] P. Cao, M. Qian, D.H. St John, Scripta Mater. 51 (2004) 647–651.
[20] A. Luo, M. Pekguleryuz, J. Mater. Sci. 29 (1994) 5259–5271.
[21] H. Zheng, S. Wu, H. Sheng, C. Liu, Y. Liu, F. Cao, Z. Zhou, X. Zhao, D. Zhao, Wang,J. Appl. Phys. Lett. 104 (2014), 141906.
[22] F. Czerwinski, JOM 56 (2004) 29–31.
[23] M. Li, D.G. Xie, Evan Ma, J. Li, X.X. Zhang, Z.W. Shan, Nat. Commun. 8 (2017) 14564.
[24] Kofstad P. Elsevier Applied Science Publishers, Essex (1988).
[25] D. Alfe, M. Gillan,Phys. Rev. B 71 (2005), 220101.
[26] N. Pilling, J. Inst. Met. 29 (1923) 529–582.
[27] A. Guy, J. Hren, Elements of Physical Metallurgy, Addison-Wesley, 1974.
[28] J.A. Van Orman, K.L. Crispin, Rev. Mineral. Geochem. 72 (2010) 757–825.
[29] Y.C. Wang, B.Y. Liu, X.I. Zhao, X. Zhang, Y. Miao, N. Yang, B. Yang, L. Zhang, W. Kuang, J. Li, Nat. Commun. 9 (2018) 4058.
[30] R.T. Cygan, K. Wright, D.K. Fisler, J.D. Gale, B. Slater, Mol. Simulat. 28 (2002) 475–495.
[31] M. Isshiki, T. Irifune, K. Hirose, S. Ono, Y. Ohishi, T. Watanuki, E. Nishibori, M. Takata, M. Sakata, Nature 427 (2004) 60.
[32] R. Lindström, L.G. Johansson, G.E. Thompson, P. Skeldon, J.E. Svensson, Corros. Sci. 46 (2004) 1141–1158.
[33] B. Feng, H. An, E. Tan, Energy Fuel 21 (2007) 426–434.
[34] L.Q. Zhang, Y. Tang, Q. Peng, T. Yang, Q. Liu, Y. Wang, Y. Li, C. Du, Y. Sun, L. Cui, Nat. Commun. 9 (2018) 96.
[35] P. Turner, T.J. Bullough, R. Devenish, D. Maher, C. Humphreys, Phil. Mag. Lett. 61 (1990) 181–193.
[36] J.A. Sundararajan, M. Kaur, Y. Qiang, J. Phys. Chem. C 119 (2015) 8357–8363.
[37] S. Was Gary, Fundamentals of Radiation Materials Science, Springer, Berlin Heidelberg, 2007.